Optics Letters

Current spreading structure of GaN-based vertical-cavity surface-emitting lasers

ZHONGMING ZHENG, YUKUN WANG, YANG MEI, HAO LONG, LEIYING YING, ZHIWEI ZHENG, AND BAOPING ZHANG*

Laboratory of Micro/Nano-Optoelectronics, Department of Micro Electronic and Integrated Circuits, Xiamen University, Xiamen 361005, China
*bzhang@xmu.edu.cn

Received 30 June 2023; revised 9 August 2023; accepted 6 September 2023; posted 7 September 2023; published 28 September 2023

Indium tin oxide (ITO) is often used as a current spreading layer in the GaN-based vertical-cavity surface-emitting lasers (VCSELs). However, the absorption coefficient of ITO is significant, which reduces the laser output power, raises the threshold, and makes VCSELs hardly lase in the ultraviolet range. To find a transparent conductive structure that can replace ITO, we propose a periodic p-AlGaN/u-GaN/p-GaN structure. In the simulation of light-emitting diodes, the optimized parameter is obtained with multi-period 10 nm p-$Al_{0.1}Ga_{0.9}N$/2 nm u-GaN/8 nm p-GaN combined with n-GaN/n-$Al_{0.2}Ga_{0.8}N$ in the n region. Applying the structure to 435 nm VCSELs and comparing it to a common VCSEL with the ITO current spreading layer, it can be found that the new structure reduces the threshold from 9.17 to 3.06 kA/cm^2. The laser power increases from 1.33 to 15.4 mW. The optimized structure has a high laser power and a lower threshold, which can be used in future investigations.

https://doi.org/10.1364/OL.499036

Group-III nitrides have high-temperature tolerance, radiation resistance, high thermal conductivity, high breakdown voltage, and tunable bandgap. They have been used in vertical-cavity surface-emitting lasers (VCSELs). Nitride VCSELs are Fabry–Perot cavities, and the intracavity contacts should be transparent. In the n region, highly conductive n-type nitrides can be used as transparent contacts. However, in the p region, the doping level of p-type nitrides is too low, resulting in low conductivity and poor lateral current spreading in the devices. To improve this problem, many researchers use indium tin oxide (ITO) as a transparent conductive layer to spread the current [1–5]. However, ITO has strong absorption, even in the visible range (2000 cm^{-1}) [6]. The strong absorption reduces the laser output power and increases the threshold. It makes electrically pumped VCSELs hardly lase in the ultraviolet range [7], even though optically pumped VCSELs have realized the lasing at 275.9 nm [8]. To improve the impact of ITO absorption, GaN tunnel junction (TJ) [6,9–11], AlGaN-enhanced TJ [12], and PNP-GaN [13,14] structures were proposed. For the TJ structure, the highly conductive n-type nitrides replace the ITO, significantly reduce the threshold from 8 to 3.5 kA/cm^2, and increase the laser power from 80 to 550 μW [6]. The AlGaN-enhanced TJ further reduced the operating voltage by 0.4 V and increased the wall-plug efficiency (WPE) by 10%, compared with the common TJ structure [12]. The PNP-GaN structure can also reduce the optical loss and increase the output power but still requires a thin ITO layer (10 nm) [13]. The nitride TJ structures can effectively reduce the optical loss in the VCSEL but require a high p doping concentration, which is difficult in a shorter wavelength range [15].

As is well known, polarization of group-III nitrides is strong. For an AlGaN layer grown epitaxially on a relaxed GaN template, the surface charge density at the GaN/AlGaN interface that varied with the Al component is calculated (Supplement 1), as shown in Fig. 1(a). As the Al component increases, the surface charge density increases. Many oppositely charged carriers will be attracted by these bound charges, accumulating at the interface and forming two-dimensional electron gas (2DEG) or two-dimensional hole gas (2DHG) in the narrow-bandgap nitride, with a surface density of 10^{12}–10^{14} cm^{-2}. The carriers have high mobility in an undoped nitride, and mobility of the holes (electrons) reaches 170 cm^2 V^{-1} s^{-1} (1000 cm^2 V^{-1} s^{-1}) [16]. Such high concentration and mobility of carriers in an undoped nitride can greatly enhance carrier transportation along the interface.

In this work, we propose a new lateral current spreading structure for 435 nm VCSELs, as shown in Fig. 1(b). It contains a p-AlGaN/u-GaN (unintentionally doped GaN)/p-GaN superlattice (SL) structure in the p region (labeled as p-CS), which generates 2DHG, and an n-GaN/n-AlGaN structure in the n region (labeled as n-CS). The 2DHG in the SL could improve the lateral current spreading. A simplified equivalent circuit for the newly structured VCSEL is also shown in Fig. 1(b) [13]. i indicates the number of periods in the p-CS. The u-GaN layer is 2 nm, which reduces the scattering effect of impurities on the hole and increases the hole's mobility. EB is the electron barrier at the n-GaN/n-AlGaN interface, which could hinder the electron in the n-AlGaN layer from moving to the n-GaN layer and increase the electron concentration. Its resistance is R_{EB}. R_p denotes the resistance of the p-GaN-c layer. c_1–c_i denotes the resistance of the ith p-GaN layer. b_1–b_i denotes the resistance of the nth p-AlGaN layer. R is the total resistance of p-GaN, MQWs, and n-GaN. R_n is the resistance of the n-AlGaN layer. j_1 and j_2 denote the current density on two adjacent current paths passing through the pn junction, usually $j_1 > j_2$. The value of j_1/j_2

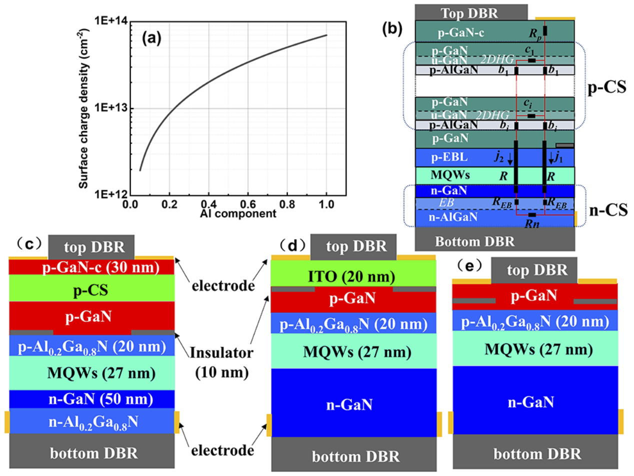

Fig. 1. (a) Surface charge density varied with the Al component at the GaN/AlGaN interface. (b) Structural diagram and the equivalent circuit for the new VCSEL. (c) Structures of VCSELs N_2–N_6, (d) R_ITO, and (e) R_GaN.

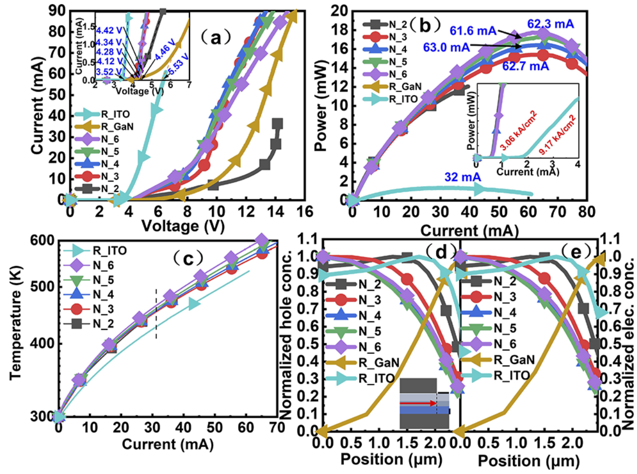

Fig. 2. (a) *I–V* and (b) *P–I* curves of N_2–N_6 and R_ITO. (c) The maximum temperature in the devices varied with the current. Normalized (d) hole and (e) electron concentration distributions along the radial direction in the last quantum well of N_2–N_6, R_GaN, and R_ITO at 0.4 mA.

is close to 1, meaning the current within the device is uniform. When $i = 1$, there is an equation

$$j_1/j_2 = 1 + \frac{c_1 + R_n}{R + R_{EB} + b_1}. \quad \textbf{(1)}$$

If the p-CS has i periods, $c_1 = \ldots = c_i$, $b_1 = \ldots = b_i$, we can get

$$j_1/j_2 = 1 + \frac{c_1/_i + R_n}{R + R_{EB} + ib_1}. \quad \textbf{(2)}$$

It can be inferred that increasing the number of periods i, reducing the resistances R_n and c_1–c_i, and increasing the resistances R_{EB} and b_1–b_i can effectively reduce the value of j_1/j_2. We first simulated a series of LED models using the software PICS3D to obtain the optimized parameters of p-CS and n-CS structures, such as the thickness and the Al component (Supplement 1). The optimized p-CS is a multi-period 10 nm p-$Al_{0.1}Ga_{0.9}N$/2 nm u-GaN/8 nm p-GaN, and the optimized n-CS is n-GaN/n-$Al_{0.2}Ga_{0.8}N$. Then, we applied the optimized p-CS and n-CS structures to a series of 435 nm VCSELs with 2, 3, 4, 5, and 6 periods of p-CS, labeled as N_2, N_3, N_4, N_5, and N_6, respectively, as shown in Fig. 1(c). The p-$Al_{0.2}Ga_{0.8}N$ layer is the electron-blocking layer (EBL). The thickness of p-GaN and n-AlGaN layers is used to adjust the position of the optical field so that the active region is aligned with the antinode of the optical field (Supplement 1). Figure 1(d) shows a reference conventional VCSEL with an ITO layer, labeled as R_ITO. To analyze the carrier distribution in a VCSEL without an ITO layer, we also simulated a VCSEL without ITO, as shown in Fig. 1(e), labeled as R_GaN.

The structure of the active region for all VCSEL models comprises 3 periods of $In_{0.15}Ga_{0.85}N$ (3 nm)/$In_{0.02}$ $Ga_{0.98}N$ (6 nm) multiple quantum wells (MQWs) [17], where the quantum barrier layer is n-doped with a concentration of $1 \times 10^{17}\,cm^{-3}$ [8], which can effectively screen the polarization electric fields [18]. The 10 nm insulating layer acts as a current confinement aperture with a diameter of 5 μm, which can be prepared by ion implantation, dry etching, and secondary growth processes. The cavity length is 3λ, and more structural parameters are shown elsewhere (Supplement 1). The electron concentration of n-GaN and n-AlGaN is $5 \times 10^{18}\,cm^{-3}$, and the hole concentration in the p region is $5 \times 10^{17}\,cm^{-3}$. SRH recombination lifetime is 20 ns, and the Auger recombination coefficient is $1 \times 10^{-31}\,cm^6 s^{-1}$ [19]. The band offset ratio is 0.7/0.3 [19]. The interface charge density is set at 50% [19]. The mobility of the electron, hole, and 2DHG is 100, 10, and 170 $cm^2V^{-1}s^{-1}$ [16], respectively. The average optical loss is set to be 10 cm^{-1} in our models [13], and the optical loss of the ITO layer is set to be 2000 cm^{-1} [6]. Self-heating is also included in our models, and the parameters are listed in Table S2 (Supplement 1).

Figure 2(a) shows the *IV* curves of these VCSELs. The turn-on voltage of R_ITO, R_GaN, N_2, N_3, N_4, N_5, and N_6 are 3.52, 5.53, 4.39, 4.12, 4.28, 4.34, and 4.42 V, respectively. It can be seen that turn-on voltages of VCSELs with the new structure are relatively large. N_3 has the lowest turn-on voltage, 4.12 V. A voltage snapback phenomenon is observed for N_4, N_5, and N_6 because carriers accumulate in the p-CS and reduce the series resistance of the devices. The snapback phenomenon might result in excessive current flowing through the devices and damage them. The *I–V* curves show a knee around 20 mA, which will be discussed below. The series resistance of each device is 50, 953, 425, 310, 264, 247Ω below 20 mA, corresponding to R_ITO, N2–N_6, respectively.

Figure 2(b) shows the *P–I* curves of each device. The threshold of R_ITO is highest, with a value of 9.17 kA/cm². However, the thresholds of the new structures, N_2–N_6, are nearly the same, with a value of 3.06 kA/cm². It is mainly because the new structure without ITO reduces the optical loss. As the current increases, the laser power increases and reaches a maximum, which results primarily from the device heating reducing the efficiency. The maximum output power for N_3, N_4, N_5, N_6, and R_ITO is 15.4, 16.4, 17.3, 17.7, and 1.33 mW, respectively, and their corresponding thermal rollover current is 62.7, 63.0, 61.6, 62.3, and 32.0 mA, respectively. The simulation of N_2 is hard to converge when the current reaches 38 mA but still can observe a lower output power than other new structures.

Figure 2(c) shows the devices' maximum temperature, located at the center of the devices (Supplement 1), varied with the current. It can be seen that, at 32 mA, the maximum temperature is 430, 456, 458, 462, and 468 K for R_ITO, N_3, N_4, N_5, and N_6, respectively. It is because the corresponding voltage increases. Figure 2(d) shows the normalized hole concentration distribution along the radial direction in the last quantum well of these VCSELs at 0.4 mA. It can be seen that the distribution of the holes in R_GaN is the most inhomogeneous, nearly 0 at the center. However, for N_3–N_6, holes are mainly distributed at the center, where N_3 has a higher hole concentration at the edge; for N_2 and R_ITO, the hole distribution at the center is around 90%. Figure 2(e) shows the normalized electron concentration distribution at the same position and current. It can be seen that the distribution is similar to the hole distribution. Carriers distributed at the center are beneficial to the lasing action.

The newly structured VCSELs have a high output power, low threshold, carrier distribution at the center, and high thermal rollover current. Among them, N_3 has the lowest turn-on voltage, device temperature, and no voltage snapback phenomenon, which is more stable, and is used to compare with R_ITO to investigate the new structure further. The simulated emission wavelengths are around 435 and 436 nm for R_ITO and N_3, respectively (Supplement 1).

Figures 3(a) and 3(b) show the band diagrams of the two devices at the edge region (2 µm from the center) at 0.4 mA. ΔE_{c1}, ΔE_{c2}, and ΔE_v are the electron barriers at the n-AlGaN/n-GaN interface, the EBL, and the barrier for a hole injection into the active region, respectively. ΔE_{c1} hinders the electron moving into the n-GaN layer and benefits the lateral current spreading (Supplement 1). The ΔE_{c2} of R_ITO is 17 meV lower than that of N_3, which indicates that the electron leakage from the active region of R_ITO will be more serious. The leaking electrons recombine with the holes in the p region and reduce the injection of the holes into the active region, significantly reducing the slope efficiency (SE). The ΔE_v of N_3 and R_ITO is nearly equal. A smaller ΔE_v benefits the holes moving into the active region and increases the hole concentration in the active region. Figures 3(c) and 3(d) show the band diagrams at 25 mA. It can be seen that ΔE_{c2} is nearly 0, which results in the electrons escaping from the active region more easily. For the new structure, the escaping electron will accumulate in the p-CS and reduce the resistance, so the *IV* curves show a knee around 20 mA.

Figures 3(e) and 3(f) show the band diagrams at 32 mA. The ΔE_{c2} of the N_3 is still nearly 0. However, the quasi-Fermi level for electrons in R_ITO is 96 meV higher than the minimum conduction band of the EBL, which causes a severe electron leakage from the active region, and hence significantly reduces the laser power, resulting in the thermal rollover current of 32 mA.

Figure 4(a) shows the hole concentration in the active region of the two devices in the edge (2 µm from the center) at 0.4 mA (the curves are shifted horizontally for clear observation). The hole concentration of N_3 is higher than that of R_ITO, and 2DHGs in the p-CS are also observed. A higher hole concentration in N_3 is because their ΔE_v is nearly equal; the p-CS generates 2DHG, which works as a hole source and increases the hole concentration.

Both hole concentrations gradually decrease toward the n-side, with the lowest hole concentration in the first well. It is because the holes have large effective masses and low mobility,

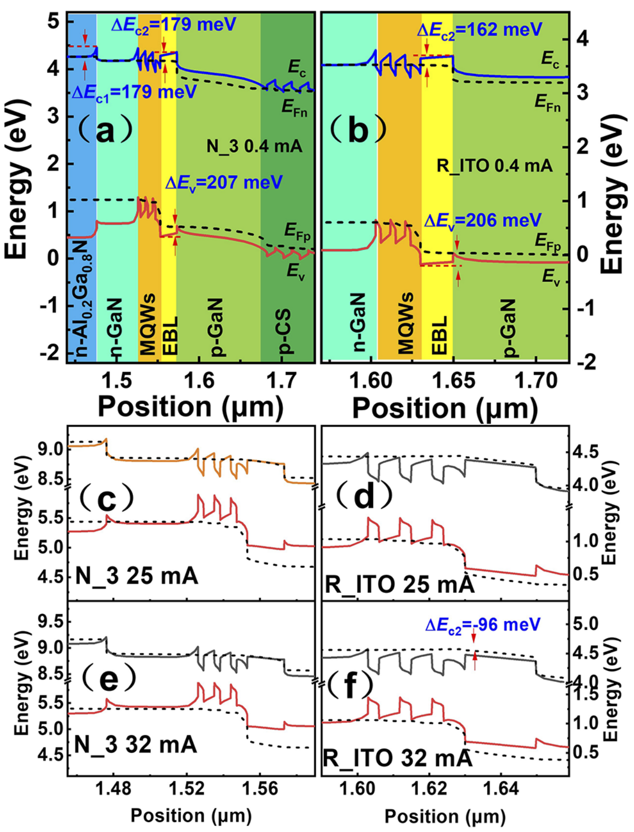

Fig. 3. Band diagrams at the edge (2 µm from the center) of (a) N_3 and (b) R_ITO at 0.4 mA. Band diagrams at the edge of (c) N_3 and (d) R_ITO at 25 and 32 mA, respectively.

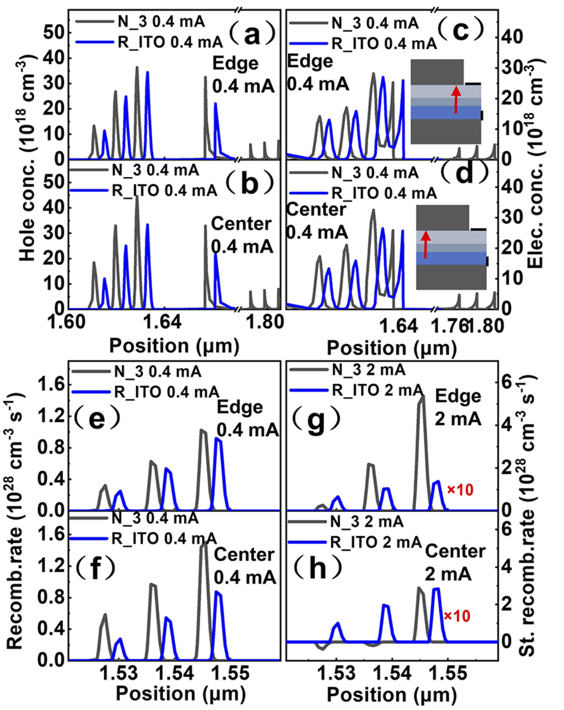

Fig. 4. Hole concentration in the active region of N_3 and R_ITO at (a) the edge and (b) central regions, respectively, at 0.4 mA. Electron concentration in the active region of N_3 and R_ITO at the (c) edge and (d) central regions, respectively, at 0.4 mA. Spontaneous radiative recombination rate in the active region of N_3 and R_ITO at the (e) edge and (f) central regions, respectively, at 0.4 mA. Stimulated radiative recombination rate in the active region of N_3 and R_ITO at the (g) edge and (h) central regions, respectively, at 2 mA.

which results in difficult transportation between the quantum wells. Figure 4(b) shows the hole concentration close to the center of the device (0.1 µm from the center) at 0.4 mA. The result is similar to that at the edge.

Figures 4(c) and 4(d) show the electron concentration in the active region of N_3 and R_ITO at the edge and central regions, respectively, at 0.4 mA. Similar to the hole distribution, the electron concentration of N_3 is higher than that of R_ITO at the edge and central regions. The electron concentration is highest in the last well for the two devices. The electrons transport quickly between quantum wells because of the small effective mass and high mobility. The EBL blocks many electrons, resulting in the accumulation of electrons in the last barrier. 2DEGs in the p-CS are also observed, which indicates the leakage of electrons accumulating in the p-CS and further enhancing the lateral current spreading.

The carrier distribution discussed above demonstrates that the proposed current spreading structure can effectively increase the device's carrier concentration. Figures 4(e) and 4(f) show the spontaneous radiative recombination rates (r_{sp}) in the active region of the two devices at the edge and central regions, respectively, at 0.4 mA. Under 0.4 mA, the r_{sp} of N_3 is higher than that of R_ITO, at the edge and central regions. It agreed with that of the carrier distribution.

Figures 4(g) and 4(h) show the stimulated radiative recombination rates (r_{st}) in the active region of both devices at the edge and central regions, respectively, at 2 mA. It can be seen that, in the two regions, the r_{st} of N_3 is much larger than that of R_ITO, and the r_{st} is larger at the last QW because of the higher carrier concentration.

The above analysis shows that the carrier concentration of N_3 is higher than that of R_ITO in each QW. It makes the spontaneous and stimulated radiative recombination rate much higher. The new structure replaces the ITO layer, significantly reducing the optical loss and threshold and increasing the laser power.

In summary, the 3-period 10 nm p-$Al_{0.1}Ga_{0.9}N$/2 nm u-GaN/8 nm p-GaN structure combined with an n-GaN/n-$Al_{0.2}Ga_{0.8}N$ structure is optimized, which can replace the ITO layer in GaN-based VCSELs. The new structure could reduce the lasing threshold from 9.17 to 3.06 kA/cm^2 and increase the output power from 1.33 to 15.4 mW. The structure can be used in future investigations.

Funding. President's Foundation of Xiamen University (20720220108); National Natural Science Foundation of China (62104204, 62234011, U21A20493); National Key Research and Development Program of China (2017YFE0131500).

Disclosures. The authors declare no conflicts of interest.

Data availability. Data underlying the results presented in this paper are not publicly available at this time but may be obtained from the authors upon reasonable request.

Supplemental document. See Supplement 1 for supporting content.

REFERENCES

1. T.-C. Lu, C.-C. Kao, and H.-C. Kuo, *et al.*, Appl. Phys. Lett. **92**, 141102 (2008).
2. M. Kuramoto, S. Kobayashi, and T. Akagi, *et al.*, Appl. Phys. Express **11**, 112101 (2018).
3. Y. Mei, G.-E. Weng, and B.-P. Zhang, *et al.*, Light: Sci. Appl. **6**, e16199 (2016).
4. G. Weng, Y. Mei, and J. Liu, *et al.*, Opt. Express **24**, 15546 (2016).
5. W.-J. Liu, X.-L. Hu, and L. Y. Ying, *et al.*, Appl. Phys. Lett. **104**, 251116 (2014).
6. J. T. Leonard, E. C. Young, and B. P. Yonkee, *et al.*, Appl. Phys. Lett. **107**, 091105 (2015).
7. Z. Zheng, Y. Wang, and J. Hoo, *et al.*, Sci. China Mater. **66**, 1978 (2023).
8. Z. Zheng, Y. Mei, and H. Long, *et al.*, IEEE Electron Device Lett. **42**, 375 (2021).
9. J. T. Leonard, E. C Young, and B. P. Yonkee, *et al.*, Proc. SPIE **9748**, 97481B (2016).
10. C.-C. Shen, Y.-T. Lu, and Y.-W. Yeh, *et al.*, Crystals **9**, 187 (2019).
11. S. Lee, C. A. Forman, and C. Lee, *et al.*, Appl. Phys. Express **11**, 062703 (2018).
12. M. S. Wong, A. Raj, and H.-M. Chang, *et al.*, AIP Adv. **13**, 015107 (2023).
13. X. Qiu, Y. Zhang, and S. Hang, *et al.*, Opt. Express **28**, 18035 (2020).
14. Z.-H. Zhang, S. T. Tan, and W. Liu, *et al.*, Opt. Express **21**, 4958 (2013).
15. J. Wang, B. K. SaifAddin, and C. J. Zollner, *et al.*, Opt. Express **29**, 40781 (2021).
16. T. T. Mnatsakanov, M. E. Levinshtein, and L. I. Pomortseva, *et al.*, Solid-State Electron. **47**, 111 (2003).
17. D. H. Hsieh, A. J. Tzou, and T. S. Kao, *et al.*, Opt. Express **23**, 27145 (2015).
18. Z. Lin, R. Hao, and G. Li, *et al.*, Jpn. J. Appl. Phys. **54**, 022102 (2015).
19. M. Usman, S. Malik, and M. A. Khan, *et al.*, Nanotechnology **32**, 215703 (2021).